The complete solution for the temperature has the form $A(x) + B(x)e^{j\omega t}$ in each medium, neglecting transients. Applying the boundary conditions of temperature and heat flux continuity at the sample surfaces ($x = 0$ and $x = -l$) and an ambient temperature T_0 at the cell walls ($x = -l - l_b$ and $x = l_g$), we can obtain the full temperature distribution throughout the cell. In particular, the a-c component of the gas temperature distribution is given by

$$\phi^{g}_{a=c}(x, t) = \Theta e^{-\sigma_g x + j\omega t}$$

where Θ represents the complex amplitude of the time-dependent temperature of the solid sample at the solid-gas boundary ($x = 0$). The explicit expression for Θ is

$$\Theta = \frac{\beta I_0}{2k_s(\beta^2 - \sigma_s^2)} \left[\frac{(r-1)(b+1)e^{\sigma_s l} - (r+1)(b-1)e^{-\sigma_s l} + 2(b-r)e^{-\beta l}}{(g+1)(b+1)e^{\sigma_s l} - (g-1)(b-1)e^{-\sigma_s l}} \right] \quad (1)$$

where $a_i = (\omega/2\alpha_i)^{1/2}$ is the thermal diffusion coefficient for medium i, $b = k_b a_b / k_s a_s$, $g = k_g a_g / k_s a_s$, $r = (1 - j)\beta/2\alpha_s$ and $\sigma_i = (1 + j)a_i$, with the subscript i taking values b, s, and g for the backing, solid, and gas, respectively. The actual time-dependent temperature distribution in the gas is given by the real part of $\phi^{g}_{a\text{-}c}$ and, as shown in Fig. 2, it attenuates rapidly to zero with increasing distance from the solid surface. Since it is effectively zero at a distance of only $2\pi/a_g$, where $1/a_g$ is the thermal diffusion length, we can effectively consider that only this thickness responds thermally to the heating of the solid.

Because of the periodic heating within it, this layer expands and contracts periodically and thus can be thought of as an acoustic piston acting on the rest of the gas column, producing an acoustic pressure signal that travels through the entire gas column (*13*). The spatially averaged temperature of the gas within this boundary layer as a function of time is

$$\bar{\phi}(t) = \frac{1}{2(2\pi)^{1/2}} \Theta e^{j(\omega t - \pi/4)}$$

Using the ideal gas law, we can approximate the displacement of this gas piston by

$$\delta x(t) = 2\pi \bar{\phi}(t)/a_g T_0$$

where we have set the average d-c temperature of the boundary layer equal to the ambient temperature T_0.

Assuming that the rest of the gas column responds adiabatically to the action of this piston, the acoustic pressure in the cell due to the displacement $\delta x(t)$ is derived from the adiabatic gas law. Thus the incremental pressure is

$$\delta p(t) = \frac{\gamma P_0}{V_0} \delta V = \frac{\gamma P_0}{l_g} \delta x(t)$$

where γ is the ratio of specific heats, P_0 and V_0 are the ambient pressure and volume, respectively, and $-\delta V$ is the incremental volume. Thus we get

$$\delta p(t) = Q e^{j(\omega t - \pi/4)}$$

for the acoustic pressure signal with the complex amplitude

$$Q = \frac{\gamma P_0 \Theta}{2^{1/2} l_g a_g T_0} \quad (2)$$

where Θ is given by Eq. 1. We therefore have a general expression for the acoustic signal in the photoacoustic cell as a function of the optical, thermal, and geometrical parameters of the system.

By applying the result to a variety of special cases we find that, for solids which are reasonably transparent to light ($\beta l < 1$), the pressure $\delta p(t)$ is proportional to βl unless the thermal diffusion length of the solid, $\mu_s = 1/a_s$, is less than l. In that case the pressure is proportional to $\beta\mu_s$.

For optically opaque solids ($\beta l \gg 1$), the pressure $\delta p(t)$ is independent of β when the thermal diffusion length μ_s is greater than the light absorption length $1/\beta$. In this case the sample, as well as being optically opaque, is also "photoacoustically opaque"—that is, the acoustic pressure is independent of the optical absorption coefficient β. However, when μ_s is less than $1/\beta$—that is, when $\beta\mu_s \ll 1$—the pressure amplitude is proportional to $\beta\mu_s$, irrespective of the magnitude of the optical absorptivity βl. Thus, even though the sample is optically opaque ($\beta l \gg 1$), it is not photoacoustically opaque—that is, the acoustic pressure is now dependent on the optical absorption coefficient β.

These results show that the photoacoustic signal is ultimately governed by the magnitude of the thermal diffusion length of the solid. Since the thermal diffusion length, μ_s, can be changed by changing the chopping frequency, ω, a solid that is completely opaque optically need not be photoacoustically opaque. It is therefore possible with the photoacoustic technique to obtain optical absorption spectra of any but the most highly opaque solids. This capability of PAS, together with its insensitivity to scattered light, makes its use as a spectroscopic tool for the investigation of solid and semisolid materials highly attractive. These features give the photoacoustic technique a unique potential for noninvasive in vivo studies of human tissues, a potential which may have important implications in biological and medical research and in medical diagnostics.

ALLAN ROSENCWAIG
ALLEN GERSHO

Bell Laboratories,
Murray Hill, New Jersey 07974

References and Notes

1. A. Rosencwaig, *Anal. Chem.* **47**, 592A (1975).
2. ———, *Opt. Commun.* **7**, 305 (1973); *Science* **181**, 657 (1973); ——— and S. S. Hall, *Anal. Chem.* **47**, 548 (1975).
3. T. H. Maugh II, *Science* **188**, 38 (1975).
4. A. G. Bell, paper presented at the 29th meeting of the American Association for the Advancement of Science, Boston, 27 August 1880. See M. Breguet, *C. R. Acad. Sci.* **91**, 595 (1880).
5. J. Tyndall, *Proc. R. Soc. London* **31**, 307 (1881).
6. W. C. Röntgen, *Philos. Mag.* **11**, 308 (1881).
7. M. E. Delaney, *Sci. Prog.* **47**, 459 (1959).
8. A. G. Bell, *Philos. Mag.* **11**, 510 (1881).
9. Lord Rayleigh, *Nature* **23**, 274 (1881).
10. W. H. Preece, *Proc. R. Soc. Lond.* **31**, 506 (1881).
11. M. E. Mercadier, *C. R. Acad. Sci.* **92**, 409 (1881).
12. J. G. Parker, [*Appl. Opt.* **12**, 2974 (1973)] also assumes that the acoustic signal is produced by heat conduction from solid to surrounding gas. His treatment, however, assumes an anomalously high absorption coefficient for a thin surface layer of the solid.
13. A more exact treatment of the pressure produced in the gas can be derived by using equations of fluid dynamics. However, the approximate procedure employed in this report gives results that are consistent with the more exact method and has the advantage of providing a simpler physical picture of the process.

7 July 1975

Laser-Excited Raman Spectroscopy for Nondestructive Partial Analysis of Individual Phases in Fluid Inclusions in Minerals

Abstract. *Laser-excited Raman spectroscopy has been successfully applied to the identification and partial analysis of solid, liquid, and gaseous phases in fluid inclusions. The procedure is no panacea for problems of analysis of fluid inclusions, but some unique features make it very useful. In particular, the measurement is performed in situ; it is nondestructive; and it can produce qualitative and quantitative data, some of which cannot be obtained otherwise, for samples as small as 10^{-9} gram.*

The analysis of fluid inclusions in minerals provides important data related to many mineralogical, geological, and geochemical processes. Inclusions represent samples of the fluids from which the host minerals have crystallized (*1*) or with which they have reacted (*2*). They may be trapped either during the growth of the host mineral or at one or more later times. Most samples thus contain more than one generation of inclusions, sometimes of greatly different ages and fluid compositions. During cooling, after the fluid has been trapped, two or more phases gener-

ally form from the originally homogeneous fluid. Most commonly, the fluid separates into liquid and gas phases; solid phases (daughter crystals) may also form. Fluid inclusions are abundant in many terrestrial samples ($\leq 10^9$ cm^{-3}) but are rarely greater than 1 mm in size. Abundance generally increases rapidly with decreasing inclusion size. The maximum amount of fluid available without ambiguity as to origin is about 10^{-6} g, and the amounts of individual constituents of interest in this fluid are frequently less than 10^{-9} g, so the analytical problems are rather severe, and many techniques have been tried (*3*), each having its own problems and limitations. Serious problems of both sample contamination and loss are introduced by all extraction procedures. Analytical data for individual inclusions of a single generation, even if only qualitative, are of more value than quantitative analyses of a mixture of inclusions from several generations. As several tests may be needed for a full identification of the various components of the inclusions, use of nondestructive methods that maintain the integrity of the samples is desirable.

Laser-excited Raman spectroscopy is a recognized tool for chemical analysis (*4*) and can record analytical quality spectra of individual particles of submicrometer dimensions (*5*). We report here its use for nondestructive in situ analysis of specific phases within single inclusions in geological samples.

The apparatus and technique were modified from those developed for the analysis of the gases present in small bubbles in glass (*6*). In essence, they consist of an optical system for focusing the beam of an argon-ion laser (operated at 514.5 nm, at powers of 10 to 100 mw) into the inclusion through one polished (or natural) face on the sample, and an efficient optical system to collect the Raman radiation scattered at approximately 90° to the direction of the incident beam (Fig. 1A). This scattered radiation is spectrally analyzed and measured by a standard Raman photoelectric double monochromator system (*6*). The incident laser beam may be focused into an effective cylindrical source volume ~7 μm in diameter and ~250 μm long. The optical collection system forms a magnified image (~ × 8) of this sample volume on the slit of the spectrometer, from which any part can be selected for analysis by masking the slit. These features reduce the Raman radiation from the host material and permit a somewhat selective sampling of the contents of the inclusion.

This optical system places constraints on the dimensions of an inclusion that can be measured. It must be reasonably equant and must be observable without obstruction from two different directions in the sample (preferably ~90° ± 30° apart). Because of these geometrical limitations, only a small fraction of the inclusions suitable for normal microscopy are suitable for this technique. In addition to these requirements, the host material should be reasonably transparent in the visible part of the spectrum (450 to 650 nm), and the contents of the inclusion should not be highly absorbing at the exciting laser wavelength. These restrictions arise primarily because the incident laser irradiance can easily approach megawatts per square centimeter.

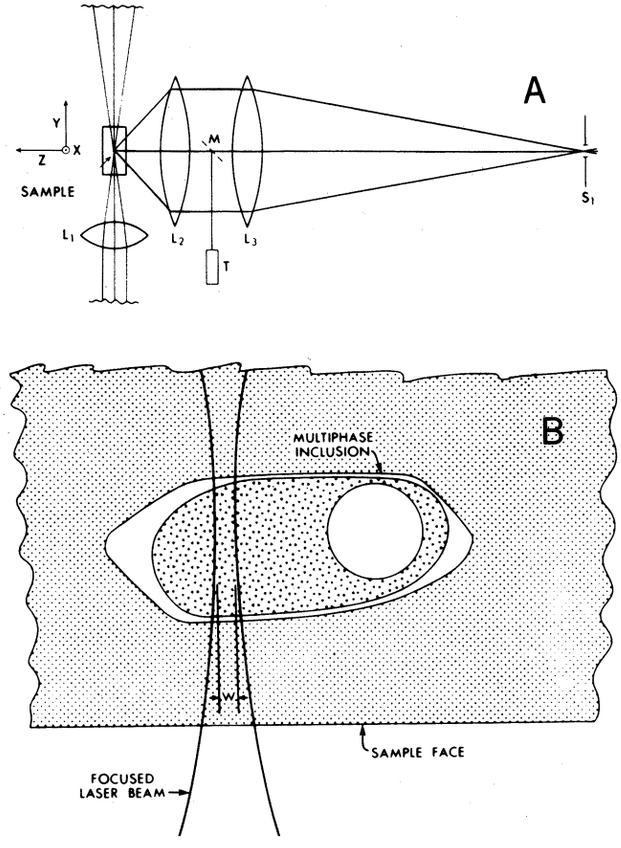

Fig. 1. (A) Diagram of the optical system used. The incident laser beam is focused into the sample by lens L_1 ($f \cong 3$ cm). Lenses L_2 ($f \cong 7.5$ cm) and L_3 ($f \cong 56$ cm) form a magnified image of the sample volume on the entrance slit (S_1) of the monochromator. Alignment was aided by use of a separate low-power He-Ne laser beam (not shown) coincident with the horizontal axis. (B) Path of the laser beam through an inclusion, as seen through the auxiliary telescope (T). The path, visible because of fluorescence and scattering, appears curved because it is the region of highest irradiance in the focused Gaussian profile beam. The minimum diameter of the "brightest" cylinder in the sample is W ($\cong 7$ μm).

The capabilities and limitations of the technique are shown in the following three analyses.

1) Fluorite, Illinois (*7*). This inclusion consists of a brine and a vapor bubble thought to contain CH_4 under pressure (Fig. 2A). Data on the sulfur content of such brines (both total concentration and species present) would be particularly relevant to the problems of formation of the Mississippi Valley–type sulfide ores. Previous microchemical analyses of similar inclusions (*8*) showed 1000 to 2000 parts per million (ppm) for total sulfur as sulfate, but these estimates were near the limit of sensitivity of the method used.

The Raman spectrum of the brine (Fig. 3A) yielded a strong characteristic spectrum for water, but no characteristic sulfate peak (~980 cm^{-1}) could be detected (*9*). A water solution with a sulfate concentration of 1000 ppm yielded a significant sulfate peak (Fig. 3B). A comparison of the two spectra, with the water peak at ~1650 cm^{-1} as an internal standard, showed the sulfate concentration in the inclusion to be definitely less than 500 ppm. This initial study and previous work (*9*) suggest that the sensitivity for measuring sulfate in aqueous inclusions could be pushed to < 100 ppm routinely. No other species was detected in the brine, including CH_4 and HS^-.

The vapor bubble was found to contain CH_4, but no other gas species were detected. The strong CH_4 line was observed at 2916.5 cm^{-1}, rather than at 2916.9 cm^{-1}, which was determined with a sample of CH_4 at 1 atm. This shift is due to pressure (*10*) and indicates that the pressure in the inclusion is 27 ± 7 atm, in agreement with previous estimates for similar inclusions by an independent destructive test (*11*).

In this sample some inconsequential turbulence was occasionally observed at the bubble-liquid interface, possibly caused by local heating due to small opaque particles adhering to the interface. In contrast, experiments on a quartz sample from Herkimer, New York (*12*) (Fig. 2C), containing inclusions that were believed to be mixtures of ethane and methane near critical density (*13*), were unsuccessful because of

heating due to absorption of the laser energy. This apparently caused polymerization of certain organic constituents in the fluid, as evidenced by precipitation of opaque material (Fig. 2C) and phase changes such as a drop in the critical temperature of the fluid.

2) Quartz, Brazil (*14*). This inclusion contains three main phases at room temperature: a water solution in contact with the walls, enclosing a globule of liquid believed to be CO_2, and a small bubble, presumably also CO_2 (Fig. 2B). The two CO_2 phases homogenize in the liquid phase (by expansion of the liquid) at 27.65°C in this and most similar inclusions in the sample.

The spectrum of the liquid CO_2 showed characteristic CO_2 bands at 1263, 1285, 1370, 1388, and 1409 cm^{-1}. Additional bands at 2328 and 2914 cm^{-1} were assigned to N_2 and CH_4. The main line of the latter is shifted down ~3 cm^{-1} from its position at atmospheric pressure (*10*). This shift is attributed to both pressure and solution effects.

The line at ~1370 cm^{-1} in liquid CO_2 originates from the species $^{13}CO_2$ (*15*). The errors involved in measuring the intensities of these lines are such that, by calibration with an appropriate CO_2 standard, the method could be used to measure a value for $\delta^{13}C$ with a precision of ± 20 parts per thousand (*16*). Although this precision is very low, the sample used here (~4 × 10^{-9} g) was about five orders of magnitude smaller than the samples used for normal $^{13}C/^{12}C$ determinations by mass spectroscopy.

The water phase, a solution having a freezing-point depression equivalent to 1*M* NaCl, showed a strong spectrum of CO_2 in solution. Reasonable extrapolations from experimental studies (*17*) show that this liquid should contain ~1.7*M* CO_2 (6.6 percent by weight). Distinguishing the CO_2 species present in water solutions is important, particularly CO_2, HCO_3^-, and CO_3^{2-}. Systematic Raman studies of these species have been published (*18*). The analysis of the Raman spectra of the brine in our sample indicates no detectable HCO_3^- or CO_3^{2-}. The reported sensitivity for CO_3^{2-} is ~75 ppm.

3) Apatite, Mexico (*19*). This sample contained a small multiphase inclusion (Fig. 2D). Among various daughter phases, the inclusion contained a crystal ~10 by 12 by 39 μm, believed to be anhydrite on the basis of its optical properties. The Raman experiment was made specifically to verify the identification of the anhydrite. Figure 3C shows the spectrum observed when the laser is focused into this crystal. The seven marked peaks appear only when the beam hits the crystal; the remainder arise from the host apatite. A comparison of these frequencies and relative intensities with those of spectra from macroscopic single crystals of anhydrite and gypsum proved that the crystal in the inclusion is anhydrite.

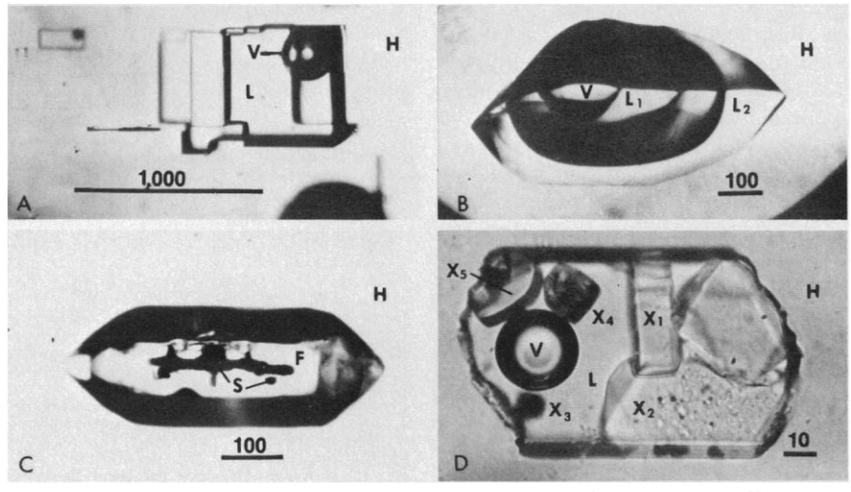

Fig. 2. Photomicrographs of inclusions in transmitted light at ~25°C. Abbreviations: *H*, host crystal; *L*, liquid; *V*, vapor; *F*, supercritical fluid; *X*, daughter mineral. Bar lengths are in micrometers. (A) Brine inclusion in fluorite; (B) CO_2-H_2O inclusion in quartz sample 28 containing liquid CO_2 (L_1) and liquid water (L_2); (C) organic supercritical fluid inclusion in quartz sample 26 (dark spots, *S*, were formed by laser irradiation); (D) inclusion in apatite having several daughter crystals (X_1, anhydrite?; X_2, halite?; X_3, magnetite?; X_4 and X_5, unidentified birefringent phases).

The results reported here show the usefulness of laser-excited Raman spectroscopy for the identification and characterization of separate phases in the nanogram (10^{-9} g) range within individual fluid inclusions, without destruction of the inclusions. The demonstration involved the detection and measurement of H_2O (as a brine); CO_2 (liquid and vapor); CH_4 (vapor); CO_2, HCO_3^-, CO_3^{2-}, and SO_4^{2-} in water solutions; N_2 and CH_4 (in CO_2 fluid); CH_4 vapor pressures; $^{13}C/^{12}C$ ratios in liquid CO_2; and anhydrite as a daughter crystal.

Certain limitations of the technique, for example, the requirement for "large," somewhat three-dimensional inclusions, arise because the instrumentation has not been specifically designed for the study of fluid inclusions. An optical system utilizing backscattered Raman radiation and higher magnification should permit application of the technique to many more of the samples normally encountered in inclusion study. The lower limit of detection of a particular constituent is controlled by the constituent itself, the background from the host material, the geometry of the inclusion, spectral interference from other constituents, and

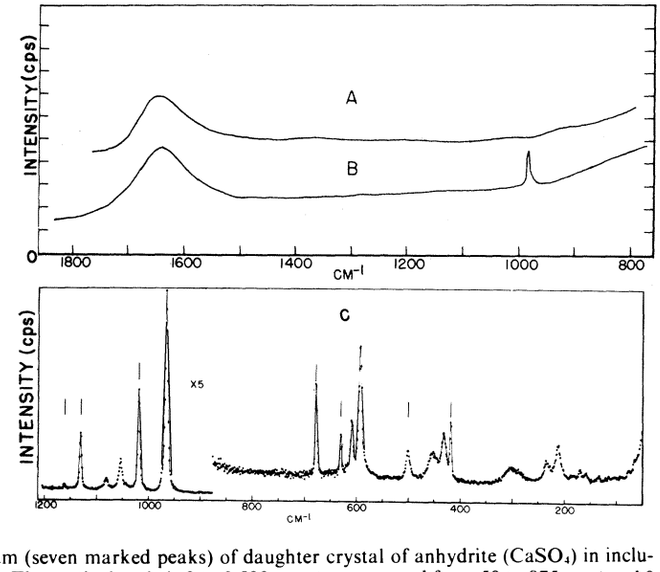

Fig. 3. (A) Raman spectrum of brine in inclusion in fluorite (Fig. 2A). The vertical scale is 100 counts per second (*cps*) per division, and the zero is shifted upward 100 counts per second. (B) Raman spectrum of water solution of $(NH_4)_2SO_4$ with a sulfate concentration of 1000 ppm by weight. The vertical scale is 300 counts per second per division, with zero on the horizontal axis. The "peak" at ~1650 cm^{-1} is the HOH bending mode of H_2O. The peak at ~980 cm^{-1} is the symmetric stretch mode of the sulfate ion. (C) Raman spectrum (seven marked peaks) of daughter crystal of anhydrite ($CaSO_4$) in inclusion in apatite (Fig. 2D). The vertical scale is 0 to 3,500 counts per second from 50 to 875 cm^{-1} and 0 to 17,500 counts per second from 875 to 1200 cm^{-1} (see text).

the ability of the phase to withstand the intense irradiance required. This last item may be the major limitation to the general applicability of the technique to smaller inclusions. Such problems can be minimized by selection of an excitation wavelength not absorbed by the sample or host.

GREGORY J. ROSASCO
National Bureau of Standards, Washington, D.C. 20234

EDWIN ROEDDER
U.S. Geological Survey, Reston, Virginia 22092

JOSEPH H. SIMMONS
National Bureau of Standards

References and Notes

1. E. Roedder, in *Geochemistry of Hydrothermal Ore Deposits*, H. L. Barnes, Ed. (Holt, Rinehart & Winston, New York, 1967), pp. 515–574.
2. For example, see B. Poty, H. A. Stalder, A. M. Weisbrod, *Schweiz. Mineral. Petrogr. Mitt.* **54** (No. 2/3), 717 (1974).
3. See E. Roedder [*U.S. Geol. Surv. Prof. Pap. 440JJ* (1972)] for a summary of the techniques used, their applicability and limitations, and the data obtained.
4. For example, see M. C. Tobin, *Laser Raman Spectroscopy: Chemical Analysis*, vol. 35; series edited by P. J. Elving and I. M. Kolthoff (Wiley-Interscience, New York, 1971); T. R. Gilson and P. J. Hendra, *Laser Raman Spectroscopy* (Wiley-Interscience, New York, 1970).
5. G. J. Rosasco, E. S. Etz, W. A. Cassatt, *Appl. Spectrosc.* **29**, 396 (1975).
6. G. J. Rosasco and J. H. Simmons, *Am. Ceram. Soc. Bull.* **53**, 626 (1974).
7. Sample ER 59-3, from Hill Mine, southern Illinois Pb-Zn-CaF_2 district; additional data are given in the caption to plate 9-3 in (*3*). The sample was recut for this test; hence it does not appear exactly as in that plate.
8. E. Roedder, B. Ingram, W. E. Hall, *Econ. Geol.* **58**, 353 (1963); E. Roedder, *Econ. Geol. Monogr.* **3**, 349 (1967).
9. S. F. Baldwin and C. W. Brown, *Water Res.* **6**, 1601 (1972).
10. A. D. May, J. C. Stryland, H. L. Welsh, *J. Chem. Phys.* **30**, 1099 (1959).
11. E. Roedder, *Schweiz. Mineral. Petrogr. Mitt.* **50**, (No. 1), 41 (1970).
12. Sample ER 61-26-13; additional data are given on p. 202 in E. Roedder, *Econ. Geol.* **58**, 167 (1963).
13. See Roedder (*3*), plates 5-6 and 5-7.
14. Sample ER 61-28b-21, part of crystal ER-61-28 from Volta Bala, Minas Gerais, Brazil; additional data are given in (*12*, pp. 172, 176, 191–194).
15. B. P. Stoicheff, *Can. J. Phys.* **35**, 608 (1957).
16. $\delta^{13}C = (R/R_S - 1) \times 1000$ (parts per mil), where R is the ratio $^{13}C/^{12}C$ in the unknown and R_S is the same ratio in a standard.
17. A. J. Ellis and R. M. Golding, *Am. J. Sci.* **261**, 47 (1963).
18. A. R. Davis and B. G. Oliver, *J. Solution Chem.* **1**, 329 (1972).
19. A gemmy honey-yellow apatite from the mineralogically well-known locality of Cerro de Mercado, Durango, Mexico, where it occurs as a late vug mineral in veins in iron deposits, associated with the sulfates alunite and gypsum. The sample was provided by S. Levine at the University of Minnesota (his sample No. CM74-53-3a).
20. We thank S. Levine for the apatite sample and H. E. Belkin for sample preparation.

7 August 1975

Planetary Brightness Changes: Evidence for Solar Variability

Abstract. *Brightness changes of Uranus and Neptune at 440 nanometers were highly correlated from 1956 to 1966. Recent observations of Saturn's satellite Titan and of Uranus and Neptune show a steady brightening at 551 and 472 nanometers since 1972. Either the solar constant is slightly variable or solar activity causes correlated changes in the albedos of planetary bodies.*

The possibility of small variations in the solar constant (the integrated solar flux per unit area as seen at the top of Earth's atmosphere) is of great importance to climatologists, solar physicists, and planetary astronomers. Currently, the uncertainty in measures of the solar constant is about ± 1 percent, and variations of that size on time scales from days to years cannot be ruled out (*1*). Limitations in the accuracy of solar constant measurements are imposed by the difficulty of maintaining the calibration of the receiver and, for ground-based measurements, the difficulty of correcting for the effects of atmospheric extinction which change with wavelength, time, and the altitude of the sun.

However, one can make differential photoelectric measurements of reflected sunlight accurate to a small fraction of 1 percent by comparing the magnitudes of the outer planets and their satellites with stars of similar brightness and color located nearby in the sky. The observations are insensitive both to the extinction, which affects all objects about equally, and to changes in the sensitivity of the photometer. Although these measurements are not easily transformed to an absolute scale of physical units, they are very suitable for the detection of small changes over a long period of time.

Two sets of photometric data, spanning 25 years, are combined in this report. Uranus and Neptune were observed at Lowell Observatory in Flagstaff, Arizona (elevation, 2210 m), continuously from 1950 to 1966. In 1972, the program was reinstated, and Titan was added as a third object. This huge satellite of Saturn was a logical addition since it is the only satellite in the solar system known to have an atmosphere, and there was good reason to suspect that its reflecting power would be constant.

Since 1972, Neptune, Uranus, and Titan have been observed regularly with the 1.1-m and 0.5-m reflecting telescopes at Lowell Observatory. Some observations of Uranus and Neptune in 1972 and 1974 were made with the 0.6-m telescope at the Mauna Kea Observatory in Hawaii (elevation, 4200 m). All observations prior to October 1973 were made by M. Jerzykiewicz and those since then by me. The same photometer, filters, and photon-counting data system have been used for all measurements.

In these observations the blue (*b*, 472 nm) and yellow (*y*, 551 nm) filters of the Strömgren narrow-band (~ 20 nm) photometric system have been used. Color effects, due to differences in the color of the comparison stars, are virtually nonexistent for such narrow bandwidths. As an experimental control, two comparison stars are used for each object and are intercompared along with the primary objects in order to ensure that they are constant in brightness. Pre- and post-opposition mean magnitudes for each object and each apparition since 1972 are shown in Fig. 1. The magnitude scale is defined in terms of published ($b - y$) colors for standard stars (*2*) and a y scale that is being defined on the basis of the Lowell observations. To simplify comparisons from year to year, all magnitudes are routinely normalized to mean opposition distances and a solar phase angle of zero (*3*, *4*).

From Fig. 1 it is clear that each object has brightened, but by different amounts, since 1972. The changes have been essentially linear with time and are highly significant, being many times larger than the annual mean errors. Variations in the brightness of Titan have been reported elsewhere, and there is also evidence that the Galilean satellites of Jupiter may have brightened from 1973 to 1974 (*5*).

The principal uncertainty in a long series of planetary observations such as these lies in the determination of the relative magnitudes of the different sets of comparison stars which must be used for each year's observations. As an example, comparison stars for Titan, two per apparition, are located at 12° (annual) intervals along the ecliptic path. Thus, considerable time and care must be invested in observing the comparison stars required for a planetary monitoring program of several years' duration.

The internal error of the mean of the differential observations for one observing period (consisting of measurements on 10 to 20 nights) is typically ± 0.001 to ± 0.002 mag, or 0.1 to 0.2 percent. External errors in the relative magnitudes of comparison stars for different years average ± 0.002 mag. Thus, the uncertainty in the resulting annual mean magnitude of a single planetary body is often as small as ± 0.003 mag or 0.33 percent. This is an order of magnitude smaller than the increases that have been observed, and so the reality of the brightening is very secure.

Further correlated changes in brightness are evident in broadband *B* (440 nm) measurements of Uranus and Neptune made